

RESEARCH ARTICLE

10.1002/2015JA021345

A new dynamic fluid-kinetic model for plasma transport within the plasmasphere

Yan Wang¹, Jiannan Tu¹, and Paul Song¹¹Space Science Laboratory and Physics Department, University of Massachusetts Lowell, Lowell, Massachusetts, USA

Key Points:

- A multispecies dynamic fluid-kinetic model for plasma transport is developed
- Effects of the flux tube convection are included in the model
- Heavy oxygen ions demonstrate different behaviors in the plasmasphere refilling

Correspondence to:

Y. Wang,
Yan_Wang@student.uml.edu

Citation:

Wang, Y., J. Tu, and P. Song (2015), A new dynamic fluid-kinetic model for plasma transport within the plasmasphere, *J. Geophys. Res. Space Physics*, 120, doi:10.1002/2015JA021345.

Received 19 APR 2015

Accepted 22 SEP 2015

Accepted article online 28 SEP 2015

Abstract A new dynamic fluid-kinetic model is developed for investigating the plasma transport along a closed magnetic flux tube in the plasmasphere by coupling the field line interhemispheric plasma (FLIP) model with a generalized semikinetic (GSK) model. The coupling is achieved via an overlapped transition region (800 km–1100 km altitude) in each of the hemispheres. The flux tube is allowed to move both radially away from, toward, and azimuthally around the Earth. In addition to H⁺, ion species O⁺ and He⁺ are for the first time treated as simulation particles in a numerical model of the plasmasphere. The simulation particles are subjected to the field-aligned electric field, magnetic mirror force, gravity, centrifugal force, and interspecies and intraspecies Coulomb collisions. The plasmaspheric refilling processes as an application of the model are studied. The simulation results show that the behaviors of O⁺ ions are substantially different from those of H⁺ and He⁺ ions.

1. Introduction

The plasmasphere is a toroidal shaped region in the inner magnetosphere dominated by cold (< 1 eV) and dense ($10^2 - 10^4 \text{ cm}^{-3}$) plasma originating from the ionosphere. The background ion species in the plasmasphere is H⁺ with variable concentrations of O⁺ and He⁺ depending on magnetospheric and ionospheric conditions. Although great progress has been made in understanding the morphology and dynamics of the plasmasphere, which was discovered in early 1960s, many questions remain unanswered, such as how Coulomb collisions and wave-particle interactions influence the plasma transport from the ionosphere to the plasmasphere during refilling, what determines relative fractions of the heavier ions in the plasmasphere, and how much plasmaspheric material, particularly heavy ions like O⁺, can be transported to the magnetopause through the plasmaspheric plumes.

In the past five decades, various numerical models have been developed to study the plasmaspheric structures and dynamics. One class of the models solved fluid equations of electrons and either single or multiple ion species [e.g., Banks *et al.*, 1971; Richards and Torr, 1990; Rasmussen *et al.*, 1993; Liemohn *et al.*, 1997; Ober *et al.*, 1997; Tu *et al.*, 2003]. For example, Rasmussen *et al.* [1993] simulated the temporal variation of the averaged plasma density based on mass conservation of the content of a flux tube with the ionosphere-plasmasphere interaction described by a parametric coupling flux model. Webb and Essex [2004] used a dynamical diffusive equilibrium approach to simultaneously simulate the field-aligned density distributions of ion species H⁺ and O⁺ for several thousands of flux tubes with ionospheric sources based on the International Reference Ionosphere (IRI) model. Several other hydrodynamic models of the plasmasphere solving mass, momentum, and energy equations have self-consistently coupled the ionosphere with the plasmasphere [e.g., Khazanov *et al.*, 1984; Richards and Torr, 1990; Tu *et al.*, 2003; Krall and Huba, 2013]. However, as pointed out by Singh and Horwitz [1992, and references therein], these fluid treatments are not suitable for studying the physics of the kinetic processes such as wave-particle interactions, hot-cold plasma interactions, and thermalization and trapping of the upflowing ions at the early-stage refilling.

While many plasmaspheric models solved fluid equations, relatively few kinetic (or semikinetic) models have been developed [e.g., Lin *et al.*, 1992; Wilson *et al.*, 1992; Miller *et al.*, 1993; Liemohn *et al.*, 1999; Reynolds *et al.*, 1999; Pierrard and Lemaire, 2001]. In these simulation models, the ionosphere was not self-consistently included because the density there is extremely high. Wilson *et al.* [1992] and Lin *et al.* [1992] used the particle simulation method to follow the motion of gyrocenters of individual H⁺ ions, in which fixed ionospheric upgoing ion fluxes of a nondrifting Maxwellian distribution were injected into the flux tube at the bases of the flux tube in both hemispheres. Miller *et al.* [1993] used a one-dimensional hybrid particle code and incorporated

a variable-flux ionospheric boundary condition at the place where the total particle flux either approached maximum for an empty flux tube or decreased to zero as the plasmaspheric density approached the saturation density. *Reynolds et al.* [1999] solved for the distribution functions of multiple-ion species by applying Liouville's theorem in the assumed collisionless plasmaspheric region.

Particle simulations are capable of studying effects of the kinetic processes which the fluid method cannot describe. However, the kinetic approach demands much more computer sources than the fluid method, in particular when used in the ionosphere where plasma densities are very high. Thus, combining the fluid method in the ionosphere with the kinetic method at higher altitudes becomes necessary. On the other hand, O^+ ions are the primary ion species in the upper ionosphere below several thousands of kilometers and present dramatically different kinetic features compared to H^+ ions because of the heavier O^+ ion mass. The relative abundance of He^+ ions is also of interest because some of the plasmaspheric ultraviolet (EUV) images are taken from He^+ resonance emission lines [*Sandel et al.*, 2001]. Therefore, O^+ and He^+ ions are needed to be treated as simulation particles in the kinetic region.

The purpose of this paper is to document the method and treatment of the new dynamic fluid-kinetic (DyFK) model, which couples a fluid model at altitudes below 800 km to a semikinetic model above it with an overlapped transition region (800 km–1100 km altitude) in both hemispheres to simulate the plasma transport along a closed field line. This model not only allows self-consistently coupling the ionospheric losses and production to a kinetic treatment of the multiple ion species ($O^+/H^+/He^+$) in the plasmasphere but also treats a closed magnetic field line including the convection of the flux tube and Coulomb collisions. An illustrative application of the new DyFK model is presented, studying the refilling processes of a depleted flux tube, particularly in the early stage of refilling when the velocity distributions are substantially deviated from Maxwellian. The new DyFK model is the first one to incorporate kinetic treatment of the heavier ions O^+ and He^+ with realistic ionospheric sources, a capability that is not possible in other existing plasmasphere simulation models. In the next section, we describe the fluid model in the ionosphere, the semikinetic treatment at high altitudes, the coupling technique between the fluid and semikinetic treatments, and the algorithm of the flux tube convection in detail. section 3 shows an application of the model, in which the kinetic features of multiple-ion species and the different behaviors of the H^+ ions and heavier ions (especially O^+ ions) during refilling are exhibited. A summary and discussion are given in section 4.

2. Simulation Method

Although the original DyFK model [e.g., *Estep et al.*, 1999; *Wu et al.*, 2002; *Tu et al.*, 2003, 2004, 2005] also couples the FLIP model to the GSK model with an overlapped transition region, it only couples the two treatments in one hemisphere to investigate the plasma transport along an open field line at high latitudes. In this study, a new DyFK model treats a closed field line by coupling the FLIP model to the GSK model with an overlapped transition region (800 km–1100 km in altitude) in each of the hemispheres, as schematically shown in Figure 1. The flux tube in the model is allowed to move both radially from near the Earth to the magnetopause and azimuthally around the Earth. The radial convection will result in variations of the length and cross-sectional area of the flux tube.

2.1. The Ionosphere Model

The FLIP model is a field-aligned time-dependent chemical-physical model of the ionosphere-plasmasphere [*Richards and Torr*, 1990; *Richards et al.*, 2000]. It solves time-dependent mass, momentum, and energy transport equations, including comprehensive chemistry for O^+ , H^+ , He^+ , N^+ , and electrons. The ion momentum equations along the magnetic field line are solved with the inertial terms ignored. The model uses the mass spectrometer and incoherent radar (MSIS-86) model [*Hedin*, 1987] to specify neutral densities and temperatures and uses the EUV flux model for aeronomic calculations [*Richards et al.*, 1994] to calculate ion photoionization rates. The neutral wind in the FLIP model can be either provided by the horizontal wind (HWM-93) model [*Hedin et al.*, 1996] or derived from the F_2 peak height provided by the international reference ionosphere (IRI-95) model [*Bilitza*, 1997]. The magnetic field in the FLIP model is assumed to be a tilted dipole.

There are several assumptions included in the FLIP model: (1) the flow velocities of all species are subsonic; (2) the relative velocity between ion species is much smaller than the average thermal velocity; (3) the velocity distributions of all charged species deviate only slightly from Maxwellian velocity distributions;

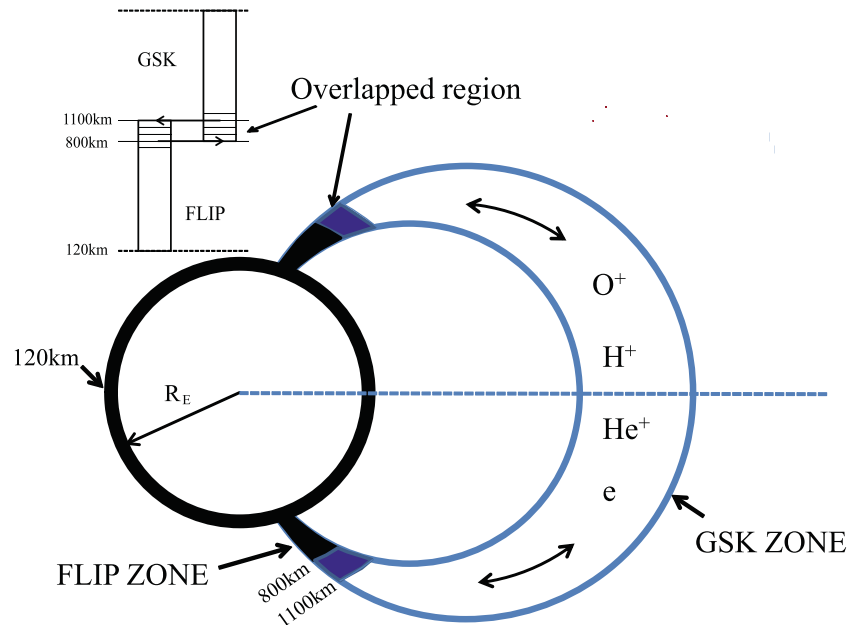


Figure 1. Schematic illustration of the DyFK model elements and the coupling transition regions between the fluid and semikinetic treatments from 800 km to 1100 km in both hemispheres.

and (4) electron and ion temperatures are both isotropic. These assumptions may be valid in the ionosphere where collisions dominate, but may not be valid in the magnetosphere, in particular in situations such as in a flux tube convecting through the plasmaspheric plume toward the magnetopause and in early stages of refilling, since the low speed assumption may no longer be valid and the velocity distributions of ions may deviate significantly away from isotropic Maxwellian distributions. The FLIP model is truncated and used for the ionospheric part in both hemispheres where the assumptions are usually valid. At higher altitudes a semikinetic treatment, which does not need restrictive assumptions about the ion velocity distributions and can treat the kinetic processes, is coupled to the truncated FLIP model.

2.2. The Semikinetic Model

The semikinetic treatment in the new DyFK model is developed based on a generalized semikinetic (GSK) simulation code [Wilson *et al.*, 1992]. The ions are treated as simulation particles and each simulation particle represents a large number of physical particles. The movements of the guiding centers of simulation particles follow a magnetic field line. Each simulation particle is subjected to the field-aligned electric field, gravitational force, magnetic mirror force, and centrifugal force from 800 km in one hemisphere to the conjugate point in the other hemisphere. The equations of motion and conservation for the gyrocenter of each simulation particle are

$$\frac{ds}{dt} = v_{\parallel} + (\mathbf{U}_c \cdot \nabla_{\perp}) s, \quad (1)$$

$$\frac{dv_{\parallel}}{dt} = \frac{q_i}{m_i} E_{\parallel} - \mathbf{g} \cdot \hat{\mathbf{b}} - \frac{\mu_i}{m_i} \frac{\partial B}{\partial s} - \mathbf{U}_c \cdot \left\{ \frac{\partial \hat{\mathbf{b}}}{\partial t} + [(-\hat{\mathbf{b}}v_{\parallel} + \mathbf{U}_c) \cdot \nabla] \hat{\mathbf{b}} \right\}, \quad (2)$$

$$\frac{d\mu_i}{dt} = \frac{d}{dt} \left(\frac{m_i v_{\perp}^2}{2B} \right) = \left[\frac{\partial}{\partial t} + (-\hat{\mathbf{b}}v_{\parallel} + \mathbf{U}_c) \cdot \nabla \right] \left(\frac{m_i v_{\perp}^2}{2B} \right) = 0, \quad (3)$$

where s is the particle position along the magnetic field line from north to south, t is the time, v_{\parallel} is the velocity antiparallel to the magnetic field, v_{\perp} is the gyrospeed, q_i and m_i are the electric charge and mass of a physical particle, respectively, of ion species i , E_{\parallel} is the electric field antiparallel to the magnetic field line, B is the magnitude of the magnetic field which is assumed to be a dipole, $\hat{\mathbf{b}} = \mathbf{B}/B$ is the unit vector of the magnetic field, \mathbf{g} is the gravitational acceleration, μ_i is the magnetic moment, and \mathbf{U}_c is the drift velocity of the flux tube at position s perpendicular to the magnetic field. The details of how to calculate \mathbf{U}_c can be found in section 2.4. The perpendicular gyrospeed in the next time step is obtained according to the conservation of the magnetic moment, equation (3).

Within the semikinetic domain, three ion species ($O^+/H^+/He^+$) are treated as particles and their bulk parameters (densities, velocities, parallel and perpendicular temperatures, and parallel and perpendicular heat fluxes) are calculated through the integration of velocity moments in the phase space. Although each simulation particle represents M_i physical particles, in the following presentations, m_i , q_i , and n_i represent those for physical particles and not simulation particles. The weight M_i is same for simulation particles of the same ion species, but is different for different species in order to prevent the number of simulation particles from being too small in a cell for each ion species and the statistical fluctuations being too large. *Wilson et al.* [1992] used the method developed by *Takizuka and Abe* [1977] to evaluate the cumulative effects of many small-angle Coulomb collisions among simulated H^+ particles with the same weight. Whereas in the present study intra-Coulomb collisions among same species and intercollisions among different species are also included through the Monte Carlo method based on the algorithm developed by *Nanbu* [1997] and *Nanbu and Yonemura* [1998], which not only groups a succession of small-angle collisions into an individual binary collision of a large scattering angle but also proposes an algorithm to evaluate Coulomb collisions among particles with different weights. *Nanbu* [1997] applied the theory to various situations and reproduced analytical results previously obtained by other authors, supporting the validity of the theory for Coulomb collisions among plasmas with the same weight. Some numerical experiments were performed by *Nanbu and Yonemura* [1998] on the temporal relaxation of temperatures and flow velocities of electrons and ions due to Coulomb collisions. They showed that the results obtained by use of different weights for each species and by use of the same weight for two species were almost identical to demonstrate the validity of their proposed weight algorithm.

On the other hand, in our model, electrons are treated as a fluid with the electron density and velocity being derived from the quasi-neutrality and parallel current-free conditions, which are mostly valid in small L regions where L is the McIlwain parameter [*McIlwain*, 1961] and is the equatorial distance of a field line in units of the Earth's radius. The electron temperature in the flux tube is assumed to be isotropic and given by an analytical expression derived by *Titheridge* [1998], which includes effects of the solar activity, day-night variations, and magnetic activity,

$$T_e(h) = T_0 \left[1 + \Psi(h) \frac{G_0}{T_0} \left(\frac{h_{eq} - h_0}{R_0^2} - \frac{h_{eq} - h}{R_h^2} \right) \right]^{2/7}, \quad (4)$$

where

$$\Psi(h) = \frac{0.05}{2L - R_0} \left[88 + \log \frac{h}{h_0} \left(10.5 - \log \frac{h}{h_0} \right) \right] \quad (5)$$

and h is the altitude, $R_h = 1 + h/R_E$, $R_0 = 1 + h_0/R_E$, $h_{eq} = (L - 1)R_E$, and R_E is the radius of the Earth. Subscript 0 denotes values at the reference height $h_0 = 400$ km. The electron temperature T_0 and its gradient G_0 ($G_0 = dT_e/dh$) are given by the least squares fits to observations [*Titheridge*, 1998]. A self-consistent solution of the electron temperature by solving time-dependent energy equations will be included in the future development of the DyFK model.

In addition, the parallel electric field generated in the semikinetic domain is calculated using the formula given by *Mitchell et al.* [1992]

$$E_{\parallel} = \frac{1}{S} \sum_j q_j \left\{ \frac{\partial}{\partial s'} (n_j V_{j\parallel}^2) - \frac{n_j V_{j\parallel}^2}{B} \frac{\partial B}{\partial s'} + \frac{g n_j}{s'^2} + \frac{\partial J}{\partial t} \frac{1}{A} + \frac{k_B}{m_j} \left[\frac{\partial (n_j T_{j\parallel})}{\partial s'} - \frac{n_j (T_{j\parallel} - T_{j\perp})}{B} \frac{\partial B}{\partial s'} \right] \right\}, \quad (6)$$

where $S = \sum_j n_j e^2 / m_j$, \sum_j runs over all ion species (O^+ , H^+ , and He^+) and electrons, s' is the arc length along the magnetic field line in reference to the 800 km altitude in the northern hemisphere, A is cross-sectional area of the flux tube which varies with $1/B$, e is the electron charge, n_j and $V_{j\parallel}$ are the number density and parallel bulk velocity of species j , q_j is the electric charge of species j , which includes electrons and multiple-ion species, J is the field-aligned current, the sum of which is assumed to be zero in the present study and then the value of A has no effect on the result of the electric field, $T_{j\parallel}$ and $T_{j\perp}$ are the parallel and perpendicular temperatures of species j , respectively, and k_B is the Boltzmann constant. In the semikinetic domain, the parallel and perpendicular temperatures of ion species are calculated through the integration of the second moment in the phase space, but the electron temperature is given by the empirical model equation (4) [*Titheridge*, 1998] and assumed to be isotropic. *Mitchell et al.* [1992] derived equation (6) from the 13-moment fluid equations under the quasi-neutrality assumption and used it to calculate the parallel electric field along the high-latitude open field line. Equation (6) can be applied not only to the open field lines but also to the closed field lines. The treatment to derive equation (6) is consistent with the treatment of electrons in our present model. Under the

quasi-neutrality and current-free conditions, the results from equation (6) are approximately equal to those calculated by a simple ambipolar electric field. *Mitchell et al.* [1992] has shown that equation (6) can be used to investigate the situations in which the current is not zero. The case including nonzero field-aligned current will be tested in our future work. Thus, we use equation (6) in the code to calculate the parallel electric field.

The Coulomb collision algorithm developed by *Nanbu and Yonemura* [1998] cannot be used to simulate the interactions between electrons and ions, since the electrons are treated as a fluid in our model. The ion heating by elastic Coulomb collisions with electrons in the semikinetic domain is simulated by a parameterized method, in which the parallel or perpendicular heating rate is [*Banks and Kockarts, 1973*]

$$\Gamma_{i\parallel,\perp} = 7.7 \times 10^{-6} n_e \left[(T_e - T_{i\parallel,\perp}) / a_i T_e^{3/2} \right], \quad (7)$$

where $\Gamma_{i\parallel,\perp}$ is in units of eV s^{-1} , a_i is the atomic mass of ion species i ($\text{O}^+/\text{H}^+/\text{He}^+$), subscripts e and i denote electrons and ion species i , respectively. The effect of ion heating by thermal electrons is not included in the refilling simulations, since the velocity distributions are substantially deviated from Maxwellian in the early stage of refilling. Whereas in some applications, such as the simulations of the daily variations of a nearly equilibrium flux tube, the ion heating by thermal electrons is implemented as follows. In each time step, we calculate the parallel and perpendicular heating rates for each ion species by substituting the temperatures of ion species and electrons into equation (7). Random fluctuations δW_{\parallel} and δW_{\perp} in the ion parallel and perpendicular energies, respectively, due to thermal fluctuations sampled from a Gaussian distribution $P(\delta W_{\parallel,\perp}) = \exp(-\delta W_{\parallel,\perp}^2 / 2\sigma_{\parallel,\perp}^2) / 2\pi\sigma_{\parallel,\perp}$ are given to each particle, where the width of the thermal spread $\sigma_{\parallel,\perp} = 1.14\Gamma_{i\parallel,\perp}\Delta t$, and Δt is the time step. The updated ion parallel velocity, $v_{\parallel f}$, and the perpendicular energy, $W_{\perp f}$, used in the next time step, then, are

$$v_{\parallel f} = v_{\parallel} \pm \sqrt{2\delta W_{\parallel} / m_i}, \quad (8)$$

and

$$W_{\perp f} = W_{\perp} + \delta W_{\perp} + 2 \cdot \sqrt{W_{\perp} \cdot \delta W_{\perp}} \cdot \cos \theta, \quad (9)$$

where v_{\parallel} and $W_{\perp} = \frac{1}{2}m_i v_{\perp}^2$ are the parallel velocity and perpendicular energy defined in equations (1) to (3), respectively, and θ is a random angle uniformly distributed between 0 and 2π . Further discussions can be found in *Su et al.* [1998] and *Estep et al.* [1999].

At each time step, the positions and velocities of simulation particles are calculated by the following procedures: First, the positions and velocities of simulation particles are calculated by the equations (1)–(3), as the particles move along the magnetic field line after one collision and before the next collision; Second, at each collision, either an intra-Coulomb collision between the same ion species or an inter-Coulomb collision between two different ion species, the velocities change via the Monte Carlo method while the energy and momentum are conserved before and after the collision but the particle positions are not altered during a collision; Third, the parallel velocities and the gyrospeeds are changed through equations (8) and (9), if the effect of ion heating by thermal electrons is included.

2.3. Coupling Transition Region

The FLIP model provides dynamic ionospheric processes. We take the density n_{i0} , field-aligned velocity $V_{\parallel i0}$, and temperatures T_{i0} from the FLIP model, where i represents O^+ , H^+ , or He^+ , at 800 km altitude in both hemispheres as input parameters for gyroaveraged drift Maxwellian velocity distributions of three ion species (O^+ , H^+ , and He^+) at 800 km altitude, which are used in the semikinetic simulation,

$$f_i(v_{\parallel}, v_{\perp}) = \frac{n_{i0}}{(2\pi)^{1/2}} \left(\frac{m_i}{k_B T_{i0}} \right)^{3/2} v_{\perp} \exp \left\{ -\frac{m_i \left[(v_{\parallel} - V_{\parallel i0})^2 + v_{\perp}^2 \right]}{2k_B T_{i0}} \right\}. \quad (10)$$

The simulation particles with upward velocities are then injected into the semikinetic domain through the Monte Carlo method, which was described in detail by *Aldrich* [1985]. The bulk parameters (densities, parallel bulk velocities, temperatures, and heat fluxes of each species) and their gradients along the field line derived

from the semikinetic simulation at 1100 km in each hemisphere are then used as the upper boundary conditions of the FLIP model. The overlapped region (800 km–1100 km in altitude) as shown in Figure 1 allows dynamic adjustments in the parameters in both simulation domains in order to maintain a smooth connection between the solutions from the two parts of the coupled model. Further details of the coupling technique are described in *Estep et al.* [1999] and *Wu et al.* [1999]. Numerical experiments conducted by *Estep et al.* [1999] found that a length of around 300 km was adequate and desirable for the transition and is adapted accordingly in our model. The collisions in the overlapped region from 800 to 1100 km are frequent enough so that the Maxwellian velocity distributions for ions and the assumptions included in the fluid model are valid in this region. *Estep et al.* [1999] has also demonstrated that the velocity enhancement in the fluid-treated ionosphere by the soft-electron precipitation can communicate upward to the kinetic-treated magnetosphere and the two treatments in the transition region match well.

2.4. Flux Tube Convection Algorithm

For cold plasmaspheric ions (<1 eV), only $\mathbf{E} \times \mathbf{B}$ drift is included, $\mathbf{U}_c = \mathbf{E} \times \mathbf{B}/B^2$, ignoring the curvature and gradient drifts. We adopt the *Mcllwain ESD* magnetospheric convection electric potential model [*Mcllwain*, 1986] with the corotation electric potential to calculate the electric field in the equatorial plane. The last term in equation (2) is the centrifugal force due to the zonal and meridional drift velocities of the flux tube [*Northrop*, 1963; *Horwitz et al.*, 1994]. The last term of equation (1) is due to the geometrical change of the flux tube, when it convects radially away from or toward the Earth. If the flux tube simply corotates with the Earth and the magnetic dipole axis coincides with the Earth's rotation axis, this term equals zero. In the present study, the coordinate system and the magnetic field are independent of time.

The motion of the plasma guiding center perpendicular to the magnetic field line can be decomposed to a radial convection (U_{cM}) in the meridional plane and a longitudinal rotation ($U_{c\phi}$). The flux tube geometry changes associated with the meridional convection velocity, U_{cM} . Not only the orientation of the magnetic field unit vector but also the length and the volume of the flux tube change as illustrated in Figure 2. Now we use Figure 2 to illustrate the algorithm for incorporation of flux tube meridional convection in the present model. The black solid line is the surface of the Earth. The black dashed line is the lower boundary of the semikinetic domain, which is held fixed at 800 km altitude during simulation. We utilize the orthogonal curvilinear dipole coordinate system [*Rasmussen et al.*, 1993]: \hat{e}_ϕ is in the azimuthal direction, \hat{e}_q is perpendicular to the magnetic field and directed toward the Earth, and \hat{e}_p is along the magnetic field. The thick blue solid lines are aligned with the magnetic field, and q remains constant along each thick blue solid line. The blue dashed lines are perpendicular to the magnetic field, and p is same along each blue dashed line. First, we consider a poleward motion at the foot of a dipole magnetic field line. At times t and $t + \Delta t$, the flux tube are located at $q = q_1$ and $q = q_2$, respectively. The increase of the L shell value due to the meridional convection during the time interval Δt is given by $\Delta L = -U_{cMeq} \Delta t$, where U_{cMeq} is the equatorial drift velocity in the meridional plane and positive when flux tube convects toward the Earth. As the flux tube moves to a larger L value, the length of the flux tube increases so that the grid points at locations 1, 2, 3, and 4 are relocated at 1', 2', 3', and 4', respectively. The cross-sectional areas of the grid cells increase due to the decrease of the magnitude of the magnetic field and the conservation of the magnetic flux. The volume of the flux tube increases accordingly with the changes in the length of the flux tube and the cross-sectional area. The plasma associated with the flux tube at $q = q_1$ remain in the same flux tube at $q = q_2$. The grid cell between grid points 2 and 3 is stretched to the new one between grid points 2' and 3' as the flux tube convects poleward; thus, the particle position s is changed by the last term ($(\mathbf{U}_{cM} \cdot \nabla_\perp) s$) of equation (1). Then the new parallel velocity of the particle is calculated by equation (2). Additional change in the particle position s is given by $v_{\parallel} \Delta t$, as the particle moves along the magnetic field line. The magnitudes of the magnetic field along the field line at $q = q_1$ and $q = q_2$ are known based on the dipolar magnetic field model. Then the gyrospeed is calculated using equation (3) because the magnetic moment of a simulation particle is conserved in the time interval Δt . In addition, grid points 1 and 4 at the lower boundary of the semikinetic domain arise to points 1' and 4', which are at an altitude above 800 km. The flux tube intersects the 800 km altitude surface at points 5 and 6. A key feature of this algorithm is that an additional portion of the field line in the semikinetic domain is pulled out of the ionosphere due to the increment of L shell, thus the high-density ionosphere appears to rise. The additional portions between points 1' (4') and 5 (6) are loaded with particles assuming the Maxwellian velocity distribution based on the parameters calculated in the fluid domain. Then the semikinetic domain is filled with particles whose positions and velocities are updated.

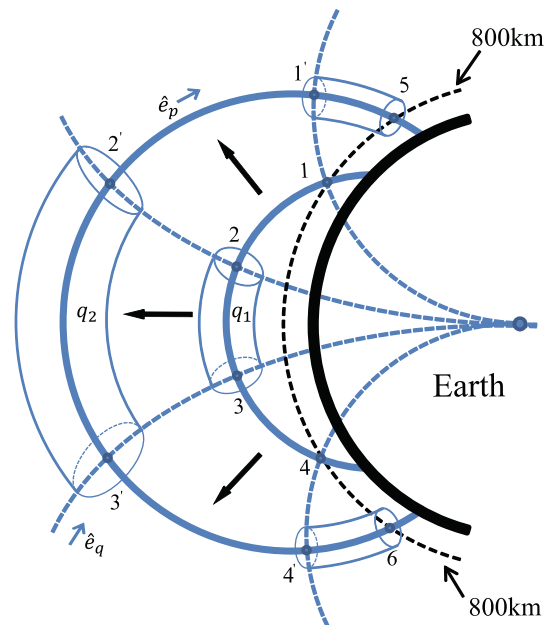


Figure 2. An illustration of the geometry change of the flux tube because of the meridional convection.

If the flux tube convects toward the Earth (from $q = q_2$ to $q = q_1$), the length of the flux tube is shortened and the volume decreases. The positions and velocities of particles are updated by equations from (1) to (3). The particles moving along the magnetic field line below 800 km are lost in the semikinetic domain. The derivations of equation (1) and the analytical expression for the centrifugal force are presented in detail in Appendix A.

There are other simulation models allowing convection of the flux tubes [Rasmussen *et al.*, 1993; Miller *et al.*, 1993; Huba *et al.*, 2000]. The effect of a change in the flux tube volume on the density as the flux tube drifts across L shell is included in Rasmussen *et al.* [1993]. Miller *et al.* [1993] incorporated the convection of the plasmaspheric tubes in a hybrid particle model. The centrifugal force (the inertial force) in the model of Miller *et al.* [1993] is derived from the fluid momentum equation by Rasmussen *et al.* [1993] and the bulk parallel velocity V_{\parallel} is used in the derivation instead of the individual particle velocity v_{\parallel} . The ionosphere is not self-consistently included and the additional portion of the field line pulled out of the ionosphere as the field line convects poleward is not taken into account in the model of Miller *et al.* [1993]. Another model of the ionosphere (SAM2) by Huba *et al.* [2000] included the $\mathbf{E} \times \mathbf{B}$ drift of a flux tube by updating the densities of each species based on conservation of the particle number and magnetic flux. The updated temperatures due to $\mathbf{E} \times \mathbf{B}$ drift were given by the equation of state. The parameter γ in the equation of state was assumed to be one.

3. Simulation Results of Plasmaspheric Refilling at $L = 4$

We now use the DyFK model to investigate the plasmaspheric refilling processes, particularly during the early stage of refilling by simulating a depleted flux tube at $L = 4$. The geophysical parameters are set as $F_{10.7} = 120$, $F_{10.7}A = 120$ (81 day average of $F_{10.7}$ centered on the day of interest), $K_p = 3$ and they remain constant during the simulation. The $L = 4$ flux tube is located inside the plasmopause as determined by the *E5D* electric field model and the corotation electric field model when $K_p = 3$ and the drift trajectory is approximately circular around the Earth. Thus, the corotation of the flux tube with the Earth is only taken into account in the present simulation. The refilling starts at 00UT (1420 LT and 1223 LT in the northern and southern hemispheres, respectively, at the footprints of the flux tube) when the densities of the three ion species and electrons are set to zero in the semikinetic domain. Again, the FLIP model results at the 800 km boundary are used to construct drift Maxwellian velocity distributions based on which the simulation particles are injected into the semikinetic domain through the Monte Carlo method [Aldrich, 1985]. The effect of the ion heating by thermal electrons is not included during the refilling process and the electron temperature in the semikinetic domain is assumed according to the Titheridge model [Titheridge, 1998]. As the flux tube corotates with the Earth, the

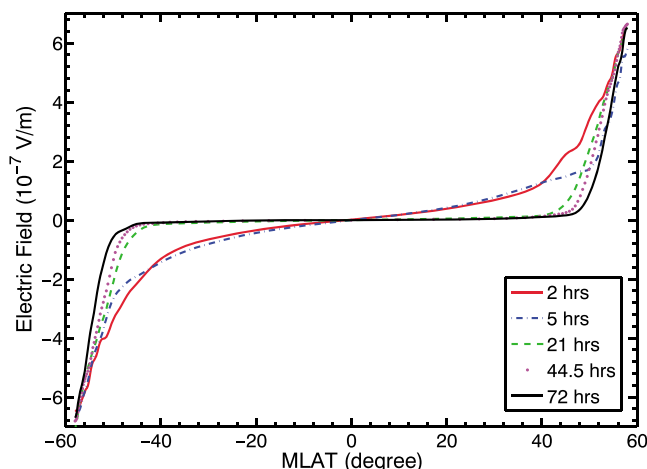


Figure 3. The parallel electric field above 800 km altitude as a function of the geomagnetic latitude at different times during refilling. The positive electric field is from the northern hemisphere to the southern hemisphere along the field line.

fluid region provides the time-varying realistic ionospheric conditions for the semikinetic domain. The kinetic features, such as the temporal evolution of the velocity distributions along the field line, during refilling are revealed by the semikinetic treatment.

3.1. Parallel Electric Field

Physically, the filling process in our model takes place as follows. Before the filling process there is no plasma, either ions or electrons above 800 km. Electrons move upward driven by the pressure gradient force as they are treated as a single fluid and are dragged down by the gravity and electric field. Ions, treated as particles, on the other hand, move upward with electron fluid to maintain the charge quasi-neutrality even if the ions are initially in hydrostatic equilibrium. The motion of an ion is determined by the kinetic energy of the particle relative to the electric and gravitational potential energies. An electric field is created in this process according to equation (6), as shown in Figure 3, in which the positive value is from the northern hemisphere to the southern hemisphere. From equation (6), the dominant term for the electric field is the pressure gradient, the first term in the square bracket, and is determined mostly by the electron pressure gradient because of the factor of reciprocal of the mass in front of the square bracket. Therefore, the parallel electric field is primarily proportional to $-T_e \nabla (\ln n_e) - \nabla T_e$ along the magnetic field line. The field-aligned electric field in the present model is directed upward and decreases with altitude in both hemispheres. During the filling, the parallel electric field, which is a function of charged particle distributions, changes both in time and in location. As the flux tube is filled with more and more particles, the electric field decreases with time due to the declining density gradients along the field line.

3.2. H⁺ Ion Refilling Processes

Figure 4 shows the parallel velocity distributions of H⁺ ions along the magnetic field line at different times during refilling. The parallel velocity distributions are calculated by binning particles according to their positions, s , and integrating the velocity distribution $f(s, v_{\parallel}, v_{\perp})$ with respect to the gyrospeed, v_{\perp} . The basic features in the H⁺ parallel velocity distributions are consistent with those presented in Figure 5 of Wilson *et al.* [1992], in which the generalized semikinetic (GSK) model was used to study the H⁺ ion refilling process of an initially empty flux tube at $L = 4$ with fixed ionospheric boundary conditions at $1.3 R_E$ geocentric distance in both hemispheres. These features included that, (1) H⁺ ions arrive at the equator from the source ionosphere after about 15 min and are accelerated to fairly high velocities (above 30 km/s) due to the parallel electric field, the mirror force, and the centrifugal force at the beginning of refilling; (2) after about 1 h, counterstreaming beams are developed along the entire flux tube and the H⁺ ion parallel bulk velocity is smaller than before, since the density gradient decreases with refilling and so does the parallel electric field (equation (6)); (3) the two beams coalesce and diffuse resulting in more particles with smaller parallel velocities via Coulomb collisions; (4) no shock is formed; (5) the two beams merge together (completely mix together to form more or less a single-peak velocity distribution) first at the low altitudes, where the density is high and Coulomb collisions are much more frequent, and gradually toward the high altitudes; and (6) when the void region in Figure 4

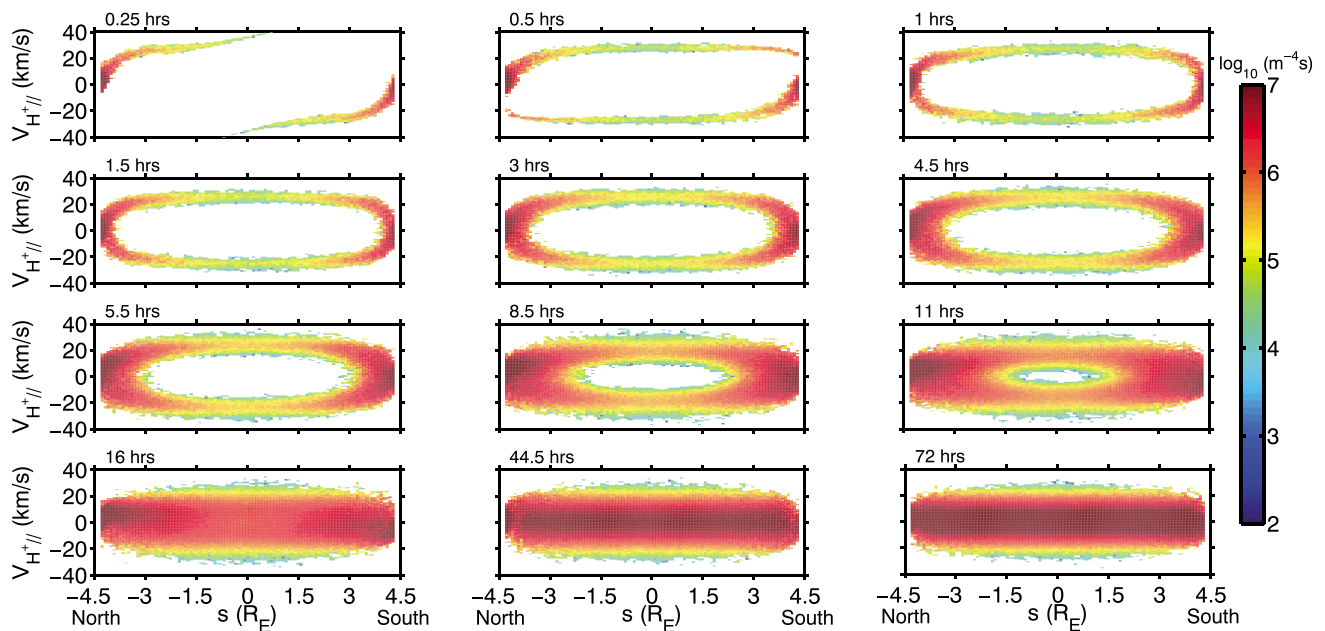


Figure 4. Parallel velocity distribution (in logarithmic scales) plots for H^+ ions at indicated times during the refilling process of an initially depleted flux tube at $L = 4$ in the semikinetic domain. The distribution is shown as a function of the parallel velocity and particle positions along the magnetic field line. The particle position, s , is negative in the northern hemisphere and positive in the southern hemisphere.

(the gap in the phase space) between the two beams is completely filled, the flux tube is still rather depleted and refilling continues.

There are, however, quantitative differences between the H^+ parallel velocity distributions given by the present study and those by *Wilson et al.* [1992], in addition to the qualitative similarities discussed above. The ionospheric boundaries are defined at 800 km and 1900 km altitude in the present model and that of *Wilson et al.* [1992], respectively. The difference in the height of the lower boundary may sound arbitrary and unimportant. However, this difference happens to coincide with the transition from O^+ dominant to H^+ dominant region as their scale heights are different. The net effects of different heights of the ionospheric boundaries, different electric potential differences between the lower boundary of the kinetic domain and the equator, and the inclusion of the centrifugal force result in a larger phase space gap of 60 km/s at the equator in the present study than the 40 km/s gap in *Wilson et al.* [1992]. The gap is filled after the two beams completely merge together at the equator after 16 h and 13.9 h in the present simulation and that of *Wilson et al.* [1992], respectively. The difference is due to the different algorithms for Coulomb collisions used in the two models in addition to the different widths of the phase gaps between the two beams.

Figure 5 shows the H^+ parallel and perpendicular temperatures above 800 km altitude along the magnetic field line at several indicated times during the refilling processes. Note that the fairly high apparent parallel temperatures in Figure 5a are due to the definition of the temperature. In our definition, the apparent temperature is calculated by the integration of the second moment in the phase space for all particles coming from both beams, although the temperature for each beam is low. At early times and in the vicinity of the equator, where the two beams are accelerated to very large and opposite parallel velocities, the H^+ apparent parallel temperatures in Figure 5a describe the bulk kinetic energies. The apparent parallel temperature decreases with time in the equatorial region in Figure 5a, as a result of Coulomb collisions which in earlier times more likely produce H^+ particles with smaller parallel velocities (e.g., after 11 h of refilling in Figure 4) and reduce parallel bulk velocities of both beams. After the two beams completely merge together at later times of refilling, the parallel temperatures represent the random thermal kinetic energies. As time proceeds, more and more H^+ particles are trapped in the flux tube and the perpendicular temperatures, in Figure 5b, increase to values near the parallel temperature. Collisions modify the H^+ velocity distributions toward isotropic first at low altitudes and gradually toward the equator, since most collisions take place at low altitudes due to the high total densities. The H^+ temperatures become nearly isotropic after 72 h of refilling in Figure 5. The time

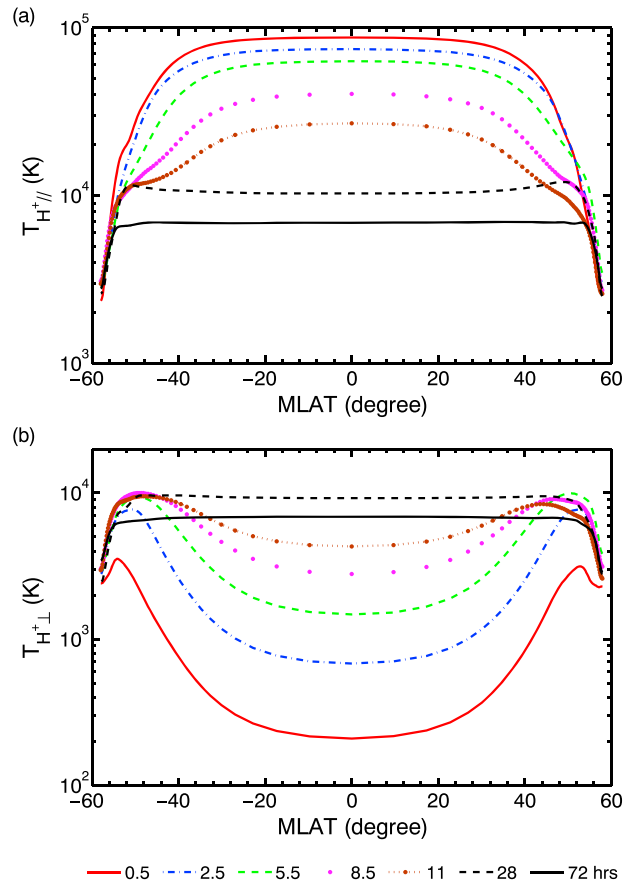


Figure 5. Distributions of (a) parallel temperatures, and (b) perpendicular temperatures of H⁺ ions along the magnetic field line in the semikinetic domain at several selected times after initiation of the refilling of a fully depleted flux tube at L = 4.

evolutions of the H⁺ parallel and perpendicular temperatures during refilling are consistent with those of Wilson *et al.* [1992].

Although one would expect the H⁺ perpendicular temperature to decrease with altitude as a result of the conservation of the magnetic moment during the early stage of refilling, it increases with altitude below 2000 km in Figure 5b. The H⁺ parallel energy is, in addition to overcome the gravity, effectively converted to the perpendicular energy below 2000 km, where the Coulomb collision frequencies of H⁺ ions are very large due to the high O⁺ densities. Therefore, the H⁺ perpendicular energy varies with the parallel energy below 2000 km, increasing with altitude. However, the Coulomb collisions above 2000 km are not as effective as below 2000 km especially at early times of refilling, because of the very low total densities at high altitudes, and the perpendicular energy decreases with the magnetic field in order to conserve the magnetic moment. In the test run in which the collisions with O⁺ ions are not included, the H⁺ perpendicular temperature (data not shown) decreases with altitude along the field line from 800 km to the equator in both hemispheres after 30 min of refilling, confirming that the perpendicular temperature increment with altitude below 2000 km is caused by the very frequent Coulomb collisions between O⁺ and H⁺ ions.

3.3. He⁺ Velocity Distributions

The He⁺ velocity distributions along the magnetic field line in the plasmasphere are now studied in simulation, although the dynamics of He⁺ ions during plasmasphere refilling have been previously studied using fluid models [e.g., Tu *et al.*, 2003; Krall *et al.*, 2008; Krall and Huba, 2013]. Figure 6 (first and second rows) shows the parallel velocity distributions and Figure 6 (third and fourth rows) the gyrospeed distributions of He⁺ ions along the magnetic field line at different times. The gyrospeed distributions are obtained by binning particles according to their positions, *s*, and their gyrospeeds, *v*_⊥, per volume. We see from Figure 6 that He⁺ ions behave similarly to the H⁺ ions in the parallel velocity distributions. Counterstreaming beams are developed along

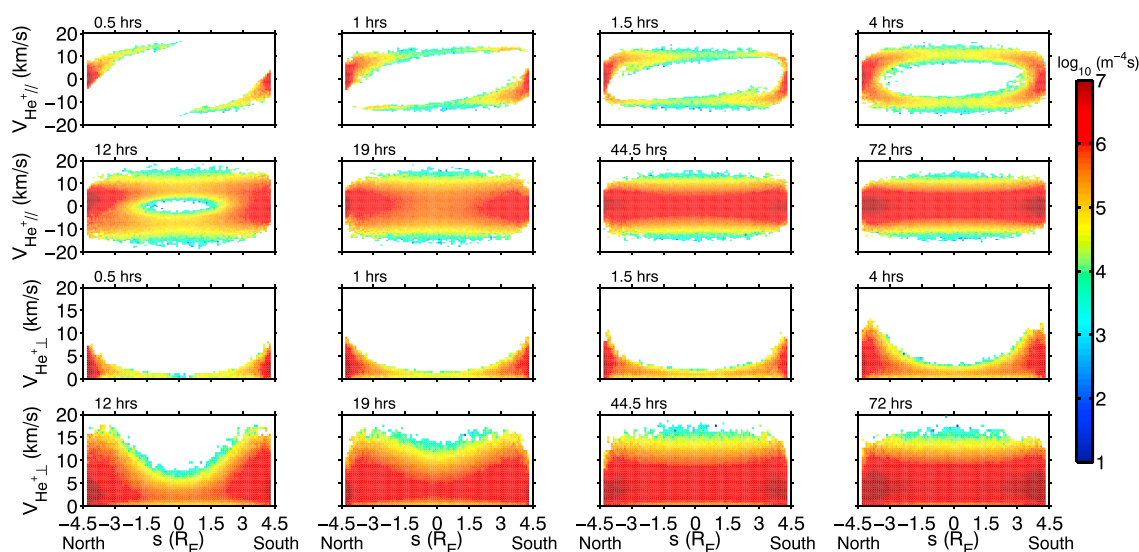


Figure 6. Velocity distribution (in logarithmic scales) plots of He⁺ particles at indicated times during the refilling process of an initially depleted flux tube at $L = 4$ in the semikinetic domain. The distribution is shown as a function of (first and second rows) the parallel velocity and (third and fourth rows) the gyrospeed and particle positions along the magnetic field line, where the particle positions are normalized to the radius of the Earth.

the flux tube and merge together first at low altitudes and gradually toward the equator. Now we study the time evolution of the gyrospeed distribution, which is, if without collisions, determined by the conservation of the magnetic moment. Because of Coulomb collisions, a fraction of the parallel energy is transferred to the perpendicular energy and the gyrospeed distribution spreads in width in the phase space, e.g., comparing the panel of the gyrospeed distribution after 12 h of refilling with the panel after 1 h of refilling in Figure 6. At later times, more and more He⁺ ions are trapped at high altitudes, so that the gyrospeed distribution further spreads at high altitudes shown by the panel after 19 h of refilling. The peak He⁺ parallel velocity appears at the equator as shown in Figure 6 (first and second rows). When the He⁺ ion becomes trapped at the equator, its peak parallel energy is converted to the perpendicular energy. The maximum perpendicular velocity appears at the equator when the system is near equilibrium, e.g., the panel after 44.5 h of refilling in Figure 6. The velocity distributions only change slightly at later times and the He⁺ temperatures (data not shown) become nearly isotropic after 47 h of refilling in a manner similar to the H⁺ ions (e.g., Figure 5). The heavier He⁺ mass results in two effects: (1) the thermal speeds of He⁺ and H⁺ ions with the temperature of 2500 K at 800 km altitude are 3.2 km/s and 6.4 km/s, respectively; (2) the acceleration for He⁺ ions due to the electric field is a quarter of that of the H⁺ ions, the first term on the right-hand side of equation (2). Thus, He⁺ ions on average take more time (15 min more) than H⁺ ions to arrive at the equator from the base of the flux tube and gain less parallel velocity than the H⁺ ions.

3.4. O⁺ Velocity Distributions

The DyFK model also, for the first time, includes O⁺ ions as particles thus the kinetic features of O⁺ ions in the plasmaspheric refilling processes can be examined. It is shown in Figure 7, in the same format as Figure 6, that the O⁺ velocity distributions are substantially different from those of H⁺ and He⁺ ions. The parallel electric field changes during refilling as shown in Figure 3 and so does the electric potential energy. Although the gravitational and centrifugal potential energies remain constant for a purely corotating field line, the total potential energy difference in O⁺ ions between the equator and 800 km altitude changes with time, which is about 2.9 eV after 1 h of refilling. The minimum parallel velocity for an O⁺ ion to reach the equator depends on its total energy, pitch angle, and the total potential energy difference between the equator and 800 km. The perpendicular energy may be transferred to the parallel energy through the mirror force when the particle moves upward. An O⁺ ion must have an upward parallel velocity with its kinetic energy greater than 2.9 eV in order to reach the equator. Otherwise, the upward O⁺ will fall back to the source ionosphere. At 2500 K, average O⁺ ions possess only 0.22 eV of thermal energy and are unable to escape. In contrast, most H⁺ and He⁺ ions have enough energy to overcome the gravity. Those O⁺ ions with high enough energy can gain parallel velocity as they move into the weaker magnetic field region, because of the magnetic moment conservation. This process can be seen in Figure 7 (the first two panels in the top row), in which the parallel

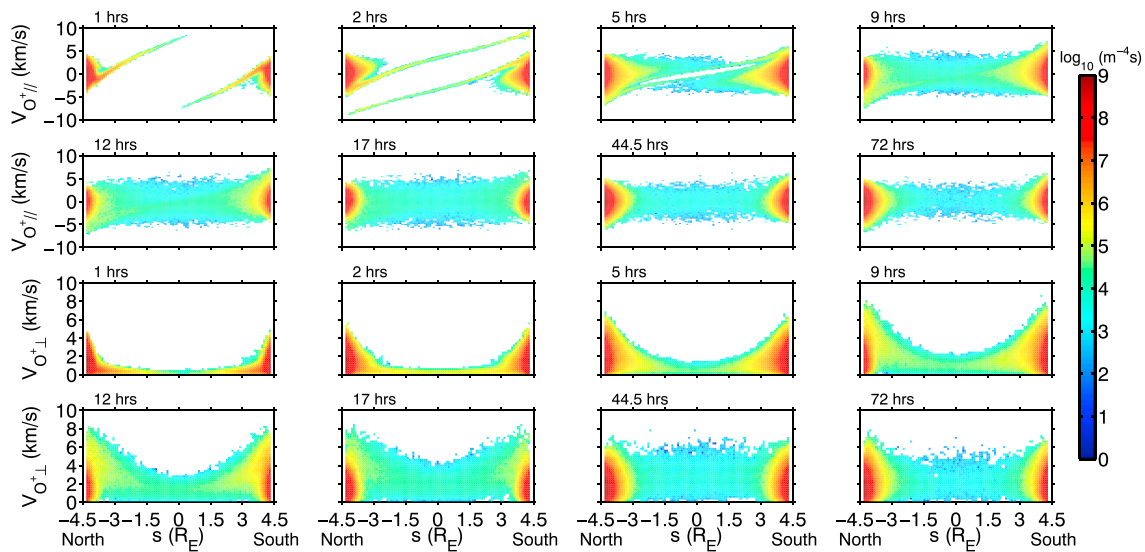


Figure 7. Same format as Figure 6 but for O⁺ particles.

velocity increases while the perpendicular energy decreases with the distance traveling from the ionosphere before reaching the equator. Once passing the equator, the O⁺ ions are accelerated downward since the gravitational force becomes greater than the sum of the mirror force and the electric field force which decreases with time when the density increases, see equation (6). The particles from each of the two hemispheres to the other hemisphere encounter but interpenetrate one another to form counterstreaming beams along the entire field line after 2 h of refilling. Most of these particles are lost from the semikinetic domain into the other hemisphere, i.e., they do not bounce back toward high altitudes. It is interesting noting that these passing particles appear to gain energy from one hemisphere to the other during the first few hours. The implied asymmetric acceleration process is due to the decrease of the electric field magnitude with time.

The O⁺ gyrospeed distributions in Figure 7 also broaden in the phase space as those of He⁺ ions in Figure 6 due to the thermalization process caused by Coulomb collisions. The thermalization process is apparent in the O⁺ parallel velocity distributions in Figure 7 (first and second rows) after 5 h of refilling. Four classes of particles were defined by *Lemaire* [1976] according to their kinetic energy and pitch angles and mentioned by *Pierrard and Lemaire* [2001]: ballistic, escaping, trapped, and incoming particles, which are all seen in our particle simulations although we may have used different terms. Most O⁺ ions emerging from the 800 km altitude ionosphere are ballistic particles, which do not have enough kinetic energy to reach the equator. If there are no Coulomb collisions, these ballistic particles arrive at certain heights below the equator and then fall back to the same side of the ionosphere. However, because of frequent collisions to these particles at lower altitudes, the pitch angles of some of these particles may change to 90° before they fall back to the ionosphere. Then these particles are trapped between the highest points they reach and the mirror points in the same hemisphere. This population increases with time as seen in Figure 7 (first and second rows). Note that the trapping of O⁺ ions is in the same hemisphere; however, the majority of trapped H⁺ and He⁺ ions bounce between mirror points in the two hemispheres. The maximum perpendicular energy of individual O⁺ ion occurs at the bottom of the flux tube as a result of the conservation of the magnetic moment and Coulomb collisions transferring the peak parallel energy to the perpendicular energy at the bottom of the flux tube, when these particles become trapped particles.

3.5. Ion Equatorial Densities and Refilling Rates

Figure 8 shows the temporal evolution of the equatorial densities of O⁺ (red), H⁺ (blue), and He⁺ (green) ions during refilling. The O⁺ and He⁺ equatorial densities are multiplied by 1000 and 10, respectively, in order to clearly show them in the same dynamic range as of the H⁺ densities. In Figure 8, the O⁺ equatorial density increases within the first 2 h of refilling, because the ionospheric escaping O⁺ particles start passing the equator as shown in Figure 7. A small number of escaping particles with larger energies arriving first and a large number of escaping particles with smaller energies coming later. Then the O⁺ equatorial density decreases with time, which can be understood by the combination of the following two effects. First, the decline of the

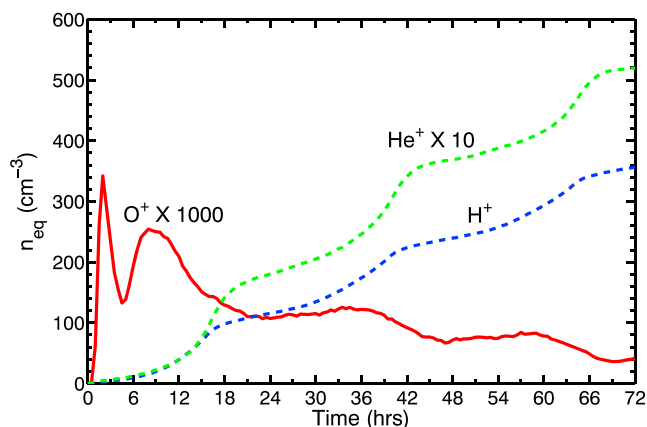


Figure 8. Time variations of the equatorial densities of H^+ , O^+ , and He^+ ions within 72 h of refilling for an initially depleted flux tube at $L = 4$. The equatorial densities of O^+ and He^+ are multiplied by 1000 and 10, respectively.

parallel electric field (equation (6)) with refilling results in that the number of escaping O^+ particles decreases with time. Second, the intraspecies and interspecies collisions encountered by the passing O^+ ions are not effective enough in producing trapped O^+ ions in the equatorial region, because of the low O^+ intraspecies collision frequency at the equator and relatively heavy mass compared with H^+ and He^+ , although collisions modify the pitch angles of O^+ particles to some extent (e.g., the thermalization shown in Figure 7).

On the other hand, the equatorial densities of H^+ and He^+ ions increase with time in Figure 8. We have run our simulation to 5 days after the initiation of refilling. H^+ and He^+ equatorial densities increase during the 5 days and have not reached saturation densities at the end of simulation. The H^+ and He^+ particles at the equator are those passing or trapped at the equator. The intraspecies and interspecies collisions encountered by passing H^+ and He^+ ions are effective enough to trap a portion of particles at the equator. A fraction of H^+ and He^+ particles are trapped at the equator through Coulomb collisions while they pass the equator every time, thus their equatorial densities increase with time as shown in Figure 8. The fluctuations of the O^+ , H^+ , and He^+ equatorial densities are due to the day-night variations of the upward ionospheric fluxes. The time variations of the field-aligned density distributions of O^+ , H^+ , and He^+ (data not shown) indicate that for each ion species, no shock is produced at any time of refilling and refilling is from the base ionospheres to the equator, consistent with the conclusions of *Wilson et al.* [1992] and observations of *Reinisch et al.* [2001, 2004], *Huang et al.* [2004], *Song et al.* [2004], and *Ozhogin et al.* [2012, 2014].

The simulated refilling rates are roughly consistent with previous observations. Numerous observed refilling rates were discussed in literatures [cf. *Denton et al.*, 2012, and references therein]. *Denton et al.* [2012] derived statistical refilling rates of the equatorial electron density over a large range of L shells based on the measurements by IMAGE Radio Plasma Imager (RPI) in passive modes [*Reinisch et al.*, 2001]. The median and mean refilling rates of the equatorial electron density given by the empirical results of *Denton et al.* [2012] for $L = 4$ were 43.7 and $46.1 \text{ cm}^{-3} \text{ d}^{-1}$, respectively. The averaged refilling rates of the electron density and mass density at the equator during 3 days in the simulation are $136.2 \text{ cm}^{-3} \text{ d}^{-1}$ and $188.3 \text{ amu/cm}^3/\text{d}$, respectively. The statistical results in *Denton et al.* [2012] were obtained from all observed rates of change of density, including negative rates (decreases in density due to azimuthal structure or radial motion or for other reasons), which may explain why the simulated refilling rate is significantly greater. *Sandel and Denton* [2007] found the local time averaged refilling rate of He^+ at equator as $17 \text{ cm}^{-3} \text{ d}^{-1}$ at $L = 4$ based on IMAGE Extreme Ultraviolet Imager (EUV) measurements during an extremely quiet period ($K_p \leq 2$) of 69 h following a moderate erosion event. The local time-averaged refilling rate of the He^+ equatorial density within 72 h of refilling in our simulation is $17.3 \text{ cm}^{-3} \text{ d}^{-1}$, which compares very well with that of *Sandel and Denton* [2007]. As shown in Figure 8, H^+ refilling rate is about 10 times greater than He^+ refilling rate, or $170 \text{ cm}^{-3} \text{ d}^{-1}$. *Reinisch et al.* [2004] studied the refilling rate after one of the biggest magnetic storms using active radio sounding of RPI. They found that the refilling of the equatorial density at $L = 3.6$ from 76 cm^{-3} to 254 cm^{-3} takes less than 14 h, translating to $305 \text{ cm}^{-3} \text{ d}^{-1}$. The high-latitude portion (higher than $\pm 45^\circ$) of the flux tubes in *Reinisch et al.* [2004] still contained much of the plasma, although the equatorial plasma density dropped to below one third of the quiet time value. However, the simulated refilling process starts from an empty flux tube above 800 km,

a significant different initial condition from the observation. Therefore, we should be cautious about the comparisons between the simulated and observed refilling rates.

4. Summary and Discussion

In this paper, we have described a newly developed DyFK model, which simulates the plasma transport along a closed magnetic field line, including the convection of the flux tube, realistically changing ionospheric conditions, multiple ion species, intraspecies, and interspecies Coulomb collisions, and anisotropic temperatures. The simulation results provide the magnetic field-aligned density distributions, bulk velocities, anisotropic temperatures of multiple ion species ($H^+/He^+/O^+$) and ion velocity distributions in the phase space. The present model has been used to study the plasmaspheric refilling processes for multiple ion species. The simulated plasmaspheric refilling processes indicate that no shock develops either at the bottom or at the top of the flux tube during early stages of refilling and the refilling is from the bottom ionosphere to the equator.

The present model can be, for example, used to study the density distributions and morphology of the plasmasphere under various solar wind/IMF conditions, the hemispheric asymmetry of the density distributions, and the effects of diurnal convection which results in flux tube compression and rarefaction. The DyFK model will be further improved in future works, such as, utilizing a more realistic magnetic field model (e.g., *Tsyganenko* magnetic model) and solving the electron energy equation to self-consistently calculate the electron temperatures. The model will be potentially used to provide 3-D descriptions of the global plasmasphere with multiple-drifting flux tubes simultaneously simulated. And it will also be applied to the simulations of the plasma transport from the plasmasphere to the dayside magnetopause through the plasmaspheric plume under disturbed geomagnetic conditions, which may have significant effects on the dayside reconnection.

Since counterstreaming beams develop along the field line at the very early stage of refilling, in principle the two-stream instability can arise. However, the two-stream instability mechanism is not included in the present model because the timescale we considered is larger than the inverse of both the ion gyrofrequency and the ion plasma frequency. We use a time step of 1 s so that the two-stream instability cannot be resolved, although at the beginning of the refilling in a very short timescale when the ion density is low (so that the ion plasma frequency is very low) the two-stream instability may develop but then quickly be smoothed out as the density increases.

The kinetic features of the O^+ and He^+ ions during refilling are for the first time presented by a numerical model of the plasmasphere. The He^+ ions behave more like the H^+ ions, but the O^+ ion behaviors are substantially different from the H^+ and He^+ ions due to their heavy masses. Most of O^+ ions are bounded by the gravitational force, bouncing back and forth above the ionosphere and below the equator. They accumulate at lower altitudes. On the other hand, H^+ and He^+ ions easily travel through the equator bouncing between two ionospheres and are trapped at high altitudes. Coulomb collisions encountered by O^+ ions help to modify the velocity distributions but are not effective enough to trap O^+ ions around the equator. Additional mechanisms such as wave-particle interactions may be needed to trap the heavy O^+ ions at high altitudes. H^+ has usually been the only ion species that is treated as particles in the simulations of the plasmasphere, although interspecies collisions also play significant roles in the kinetic processes. For example, Coulomb collisions between H^+ and O^+ ions can explain the H^+ perpendicular temperature distribution along the field line below 2000 km at the early stage of refilling, implying the importance of including multiple ion species as particles in the simulation.

Appendix A: Centrifugal Force in Dipole Coordinate System

In the present model, we assume a static dipolar magnetic field, thus

$$\frac{\partial \hat{b}}{\partial t} = 0, \quad (A1)$$

and

$$\hat{b} = -\frac{2 \cos \theta}{(1 + 3 \cos^2 \theta)^{1/2}} \hat{e}_r - \frac{\sin \theta}{(1 + 3 \cos^2 \theta)^{1/2}} \hat{e}_\theta, \quad (A2)$$

where θ is the colatitude, \hat{b} is the unit vector of the magnetic field, \hat{e}_r and \hat{e}_θ are the unit vectors in the spherical coordinate system. We adapt the orthogonal curvilinear dipole coordinates ϕ, q, p (right-handed system [Rasmussen *et al.*, 1993]) : azimuthal angle ϕ ,

$$q = \left(\frac{R_E}{r} \right) \sin^2 \theta, \quad (\text{A3})$$

and

$$p = \left(\frac{R_E}{r} \right)^2 \cos \theta, \quad (\text{A4})$$

where q is perpendicular to the magnetic field line and directed toward the Earth, p is aligned with the magnetic field, r is the geocentric distance, and R_E is the Earth's radius. Unit vectors and scale factors are [Rasmussen *et al.*, 1993]:

$$\begin{aligned} \hat{e}_\phi &= -\sin \phi \hat{e}_x + \cos \phi \hat{e}_y, \\ \hat{e}_q &= -\frac{\sin \theta}{(1 + 3 \cos^2 \theta)^{1/2}} \hat{e}_r + \frac{2 \cos \theta}{(1 + 3 \cos^2 \theta)^{1/2}} \hat{e}_\theta, \\ \hat{e}_p &= -\frac{2 \cos \theta}{(1 + 3 \cos^2 \theta)^{1/2}} \hat{e}_r - \frac{\sin \theta}{(1 + 3 \cos^2 \theta)^{1/2}} \hat{e}_\theta, \\ h_\phi &= r \sin \theta, \end{aligned} \quad (\text{A5})$$

$$\begin{aligned} h_q &= \frac{R_E}{\sin \theta (1 + 3 \cos^2 \theta)^{1/2}} \left(\frac{r}{R_E} \right)^2, \\ h_p &= \frac{R_E}{(1 + 3 \cos^2 \theta)^{1/2}} \left(\frac{r}{R_E} \right)^3, \end{aligned} \quad (\text{A6})$$

where \hat{e}_x and \hat{e}_y are unit vectors in the Cartesian coordinate system. The drift velocity can be written as [Rasmussen *et al.*, 1993]

$$\begin{aligned} \mathbf{U}_c &= h_q \frac{dq}{dt} \hat{e}_q + h_\phi \frac{d\phi}{dt} \hat{e}_\phi \\ &= -\frac{h_q}{L^2} \frac{dL}{dt} \hat{e}_q + h_\phi \frac{d\phi}{dt} \hat{e}_\phi \\ &= U_{cM} \hat{e}_q + U_{c\phi} \hat{e}_\phi \end{aligned} \quad (\text{A7})$$

where $q = 1/L$, U_{cM} is the meridional drift velocity and $U_{c\phi}$ is the azimuthal drift velocity. The analytical expression of the centrifugal force (last term in equation (2)) is given by

$$\begin{aligned} F_{cf} &= -\mathbf{U}_c \cdot \left\{ \frac{\partial \hat{b}}{\partial t} + [(\mathbf{v}_\parallel + \mathbf{U}_c) \cdot \nabla] \hat{b} \right\} = U_{cM} v_\parallel \frac{3 \sin \theta (1 + \cos^2 \theta)}{r (1 + 3 \cos^2 \theta)^{3/2}} \\ &\quad + U_{cM}^2 \frac{6 \cos \theta (1 + \cos^2 \theta)}{r (1 + 3 \cos^2 \theta)^{3/2}} + U_{c\phi}^2 \frac{3 \cos \theta}{r (1 + 3 \cos^2 \theta)^{1/2}}, \end{aligned} \quad (\text{A8})$$

where $\nabla = \hat{e}_p \frac{1}{h_p} \frac{\partial}{\partial p} + \hat{e}_q \frac{1}{h_q} \frac{\partial}{\partial q} + \hat{e}_\phi \frac{1}{h_\phi} \frac{\partial}{\partial \phi}$ and $\mathbf{v}_\parallel = -v_\parallel \hat{e}_p$.

In the semikinetic zone, s is the position of the particle on the magnetic field line, negative in the northern hemisphere and positive in the southern hemisphere with $s(\theta = \pi/2) = 0$. Since $ds = r \sqrt{1 + 3 \cos^2 \theta} / \sin \theta d\theta$ on a given dipole flux tube, then s is given as

$$s(r, \theta) = \int_{\pi/2}^{\theta} r \sqrt{1 + 3 \cos^2 \theta} / \sin \theta d\theta = -\frac{r}{\sin^2 \theta} \left[\frac{\cos \theta \sqrt{1 + 3 \cos^2 \theta}}{2} + \frac{\sqrt{3}}{6} \ln \left(\sqrt{3} \cos \theta + \sqrt{1 + 3 \cos^2 \theta} \right) \right]. \quad (\text{A9})$$

In the dipole coordinate system, s is a function of q and p . The derivative of s with respect to time is

$$\begin{aligned}
 \frac{ds}{dt} &= \frac{\partial s}{\partial p} \frac{dp}{dt} + \frac{\partial s}{\partial q} \frac{dq}{dt} \\
 &= -h_p \frac{dp}{dt} + \frac{\partial s}{\partial q} \frac{1}{h_q} U_{cM} \\
 &= v_{\parallel} + U_{cM} \hat{e}_q \cdot \nabla_q s \\
 &= v_{\parallel} + U_{cM} \hat{e}_q \cdot \nabla_q s + U_{c\phi} \hat{e}_\phi \cdot \nabla_\phi s \\
 &= v_{\parallel} + \mathbf{U}_c \cdot \nabla_{\perp} s,
 \end{aligned} \tag{A10}$$

since $\nabla_\phi s = 0$, the term $U_{c\phi} \hat{e}_\phi \cdot \nabla_\phi s$ can be added into the right-hand side of the above equation.

From equation (A7), $U_{cM} = -\frac{h_q}{L^2} \frac{dl}{dt}$ and $U_{c\phi} = h_\phi \frac{d\phi}{dt}$, the relationships between U_{cM} ($U_{c\phi}$) at any point on a given dipole field line and U_{cMeq} ($U_{c\phi eq}$) at the point where the given field line intersects with the equatorial plane are given by

$$U_{cM} = \frac{\sin^3 \theta}{(1 + 3 \cos^2 \theta)^{1/2}} U_{cMeq}, \tag{A11}$$

$$U_{c\phi} = \sin^3 \theta U_{c\phi eq}. \tag{A12}$$

The centrifugal force and the time derivative of s can be expressed in terms of the equatorial drift velocities $U_{c\phi eq}$ and U_{cMeq}

$$F_{cf} = U_{cMeq} v_{\parallel} \frac{3 \sin^4 \theta (1 + \cos^2 \theta)}{r (1 + 3 \cos^2 \theta)^2} + U_{c\phi eq}^2 \frac{3 \cos \theta \sin^6 \theta}{r (1 + 3 \cos^2 \theta)^{1/2}} + U_{cMeq}^2 \frac{6 \cos \theta \sin^6 \theta (1 + \cos^2 \theta)}{r (1 + 3 \cos^2 \theta)^{5/2}}, \tag{A13}$$

$$\frac{ds}{dt} = v_{\parallel} - U_{cMeq} \frac{\sin^4 \theta}{(1 + 3 \cos^2 \theta)} \frac{\partial s}{\partial r} + U_{cMeq} \frac{2 \cos \theta \sin^3 \theta}{r (1 + 3 \cos^2 \theta)} \frac{\partial s}{\partial \theta}. \tag{A14}$$

Acknowledgments

The work at UML was supported by NSF grants AGS-1303596 and 1248242 and NASA grant NNX12AD22G. All data in the paper can be obtained from Yan Wang (email: Yan_Wang@student.uml.edu).

Michael Liemohn thanks Fei He and one additional reviewer for their assistance in evaluating this paper.

References

- Aldrich, C. (1985), Particle code simulations with injected particles, *Space Sci. Rev.*, *42*(1-2), 131–144, doi:10.1007/BF00218228.
- Banks, P. M., and G. Kockarts (1973), *Aeronomy*, Academic Press, New York, and London.
- Banks, P. M., A. Nagy, and W. Axford (1971), Dynamical behavior of thermal protons in the mid-latitude ionosphere and magnetosphere, *Planet. Space Sci.*, *19*(9), 1053–1067, doi:10.1016/0032-0633(71)90104-8.
- Bilitza, D. (1997), International reference ionosphere—Status 1995/96, *Adv. Space Res.*, *20*(9), 1751–1754, doi:10.1016/S0273-1177(97)00584-X.
- Denton, R. E., Y. Wang, P. A. Webb, P. M. Tengdin, J. Goldstein, J. A. Redfern, and B. W. Reinisch (2012), Magnetospheric electron density long-term (> 1 day) refilling rates inferred from passive radio emissions measured by IMAGE RPI during geomagnetically quiet times, *J. Geophys. Res.*, *117*, A03221, doi:10.1029/2011JA017274.
- Estep, G. M., J. L. Horwitz, Y. J. Su, P. G. Richards, G. R. Wilson, and D. G. Brown (1999), A dynamic fluid-kinetic (DyFK) model for ionosphere-magnetosphere plasma transport: Effects of ionization and thermal electron heating by soft electron precipitation, *Terr. Atmos. Oceanic Sci.*, *10*(3), 491–510.
- Hedin, A. E. (1987), MSIS-86 thermospheric model, *J. Geophys. Res.*, *92*(A5), 4649–4662, doi:10.1029/JA092iA05p04649.
- Hedin, A. E., et al. (1996), Empirical wind model for the upper, middle and lower atmosphere, *J. Atmos. Terr. Phys.*, *58*(13), 1421–1447, doi:10.1016/0021-9169(95)00122-0.
- Horwitz, J. L., C. W. Ho, H. D. Scarbro, G. R. Wilson, and T. E. Moore (1994), Centrifugal acceleration of the polar wind, *J. Geophys. Res.*, *99*(A8), 15,051–15,064, doi:10.1029/94JA00924.
- Huang, X., B. W. Reinisch, P. Song, J. L. Green, and D. L. Gallagher (2004), Developing an empirical density model of the plasmasphere using IMAGE/RPI observations, *Adv. Space Res.*, *33*(6), 829–832, doi:10.1016/j.asr.2003.07.0074.
- Huba, J. D., G. Joyce, and J. A. Fedder (2000), Sami2 is Another Model of the Ionosphere (SAMI2): A new low-latitude ionosphere model, *J. Geophys. Res.*, *105*(A10), 23,035–23,053, doi:10.1029/2000JA000035.
- Khazanov, G., M. Koen, Y. Konikov, and I. Sidorov (1984), Simulation of ionosphere-plasmasphere coupling taking into account ion inertia and temperature anisotropy, *Planet. Space Sci.*, *32*(5), 585–598, doi:10.1016/0032-0633(84)90108-9.
- Krall, J., and J. D. Huba (2013), SAMI3 simulation of plasmasphere refilling, *Geophys. Res. Lett.*, *40*(11), 2484–2488, doi:10.1002/grl.50458.
- Krall, J., J. D. Huba, and J. A. Fedder (2008), Simulation of field-aligned H^+ and He^+ dynamics during late-stage plasmasphere refilling, *Ann. Geophys.*, *26*(6), 1507–1516, doi:10.5194/angeo-26-1507-2008.
- Lemaire, J. (1976), Rotating ion-exosphere, *Planet. Space Sci.*, *24*, 975–985, doi:10.1016/0032-0633(76)90009-X.
- Liemohn, M. W., G. V. Khazanov, T. E. Moore, and S. M. Guiter (1997), Self-consistent superthermal electron effects on plasmaspheric refilling, *J. Geophys. Res.*, *102*(A4), 7523–7536, doi:10.1029/96JA03962.
- Liemohn, M. W., G. V. Khazanov, P. D. Craven, and J. U. Kozyra (1999), Nonlinear kinetic modeling of early stage plasmaspheric refilling, *J. Geophys. Res.*, *104*(A5), 10,295–10,306, doi:10.1029/1999JA900104.

- Lin, J., J. L. Horwitz, G. R. Wilson, C. W. Ho, and D. G. Brown (1992), A semikinetic model for early stage plasmasphere refilling: 2, Effects of wave-particle interactions, *J. Geophys. Res.*, *97*(A2), 1121–1134, doi:10.1029/91JA02729.
- McIlwain, C. E. (1961), Coordinates for mapping the distribution of magnetically trapped particles, *J. Geophys. Res.*, *66*(11), 3681–3691, doi:10.1029/JZ066i011p03681.
- McIlwain, C. E. (1986), A Kp dependent equatorial electric field model, *Adv. Space Res.*, *6*(3), 187–197, doi:10.1016/0273-1177(86)90331-5.
- Miller, R. H., C. E. Rasmussen, T. I. Gombosi, G. V. Khazanov, and D. Winske (1993), Kinetic simulation of plasma flows in the inner magnetosphere, *J. Geophys. Res.*, *98*(A11), 19,301–19,313, doi:10.1029/93JA01292.
- Mitchell, H. G., S. B. Ganguli, and P. J. Palmadesso (1992), Diodelike response of high-latitude plasma in magnetosphere-ionosphere coupling in the presence of field-aligned currents, *J. Geophys. Res.*, *97*(A8), 12,045–12,056, doi:10.1029/92JA00796.
- Nanbu, K. (1997), Theory of cumulative small-angle collisions in plasmas, *Phys. Rev. E*, *55*, 4642–4652, doi:10.1103/PhysRevE.55.4642.
- Nanbu, K., and S. Yonemura (1998), Weighted particles in Coulomb collision simulations based on the theory of a cumulative scattering angle, *J. Comput. Phys.*, *145*(2), 639–654, doi:10.1006/jcph.1998.6049.
- Northrop, T. G. (1963), *The Adiabatic Motion of Charged Particles*, Interscience Publ., New York.
- Ober, D. M., J. L. Horwitz, and D. L. Gallagher (1997), Formation of density troughs embedded in the outer plasmasphere by subauroral ion drift events, *J. Geophys. Res.*, *102*(A7), 14,595–14,602, doi:10.1029/97JA01046.
- Ozhogin, P., J. Tu, P. Song, and B. W. Reinisch (2012), Field-aligned distribution of the plasmaspheric electron density: An empirical model derived from the IMAGE RPI measurements, *J. Geophys. Res.*, *117*, A06225, doi:10.1029/2011JA017330.
- Ozhogin, P., P. Song, J. Tu, and B. W. Reinisch (2014), Evaluating the diffusive equilibrium models: Comparison with the IMAGE RPI field-aligned electron density measurements, *J. Geophys. Res.*, *119*, 4400–4411, doi:10.1002/2014JA019982.
- Pierrard, V., and J. Lemaire (2001), Exospheric model of the plasmasphere, *J. Atmos. Sol. Terr. Phys.*, *63*(11), 1261–1265, doi:10.1016/S1364-6826(00)00227-3.
- Rasmussen, C. E., S. M. Guiter, and S. G. Thomas (1993), A two-dimensional model of the plasmasphere: Refilling time constants, *Planet. Space Sci.*, *41*(1), 35–43, doi:10.1016/0032-0633(93)90015-T.
- Reinisch, B. W., X. Huang, P. Song, G. S. Sales, S. F. Fung, J. L. Green, D. L. Gallagher, and V. M. Vasyliunas (2001), Plasma density distribution along the magnetospheric field: RPI observations from IMAGE, *Geophys. Res. Lett.*, *28*(24), 4521–4524, doi:10.1029/2001GL013684.
- Reinisch, B. W., X. Huang, P. Song, J. L. Green, S. F. Fung, V. M. Vasyliunas, D. L. Gallagher, and B. R. Sandel (2004), Plasmaspheric mass loss and refilling as a result of a magnetic storm, *J. Geophys. Res.*, *109*, A01202, doi:10.1029/2003JA009948.
- Reynolds, M. A., G. Ganguli, J. A. Fedder, J. Lemaire, R. R. Meier, and D. J. Meléndez-Alvira (1999), Thermal plasmaspheric morphology: Effect of geomagnetic and solar activity, *J. Geophys. Res.*, *104*(A5), 10,285–10,294, doi:10.1029/1999JA900050.
- Richards, P. G., and D. G. Torr (1990), Auroral modeling of the 3371 Å emission rate: Dependence on characteristic electron energy, *J. Geophys. Res.*, *95*(A7), 10,337–10,344, doi:10.1029/JA095iA07p10337.
- Richards, P. G., J. A. Fennelly, and D. G. Torr (1994), EUVAC: A solar EUV flux model for aeronomic calculations, *J. Geophys. Res.*, *99*(A5), 8981–8992, doi:10.1029/94JA00518.
- Richards, P. G., et al. (2000), On the relative importance of convection and temperature to the behavior of the ionosphere in North America during January 6–12, 1997, *J. Geophys. Res.*, *105*(A6), 12,763–12,776, doi:10.1029/1999JA000253.
- Sandel, B. R., and M. H. Denton (2007), Global view of refilling of the plasmasphere, *Geophys. Res. Lett.*, *34*, L17102, doi:10.1029/2007GL030669.
- Sandel, B. R., R. A. King, W. T. Forrester, D. L. Gallagher, L. Dennis, A. L. Broadfoot, and C. C. Curtis (2001), Initial results from the IMAGE extreme ultraviolet imager, *Geophys. Res. Lett.*, *28*(8), 1439–1442, doi:10.1029/2001GL012885.
- Singh, N., and J. L. Horwitz (1992), Plasmasphere refilling: Recent observations and modeling, *J. Geophys. Res.*, *97*(A2), 1049–1079, doi:10.1029/91JA02602.
- Song, P., B. W. Reinisch, and X. Huang (2004), Magnetospheric active wave measurements, *COSPAR Colloquia Ser.*, *16*, 235–246.
- Su, Y. J., J. L. Horwitz, G. R. Wilson, P. G. Richards, D. G. Brown, and C. W. Ho (1998), Self-consistent simulation of the photoelectron-driven polar wind from 120 km to 9 R_E altitude, *J. Geophys. Res.*, *103*(A2), 2279–2296, doi:10.1029/97JA03085.
- Takizuka, T., and H. Abe (1977), A binary collision model for plasma simulation with a particle code, *J. Comput. Phys.*, *25*(3), 205–219, doi:10.1016/0021-9991(77)90099-7.
- Titheridge, J. E. (1998), Temperatures in the upper ionosphere and plasmasphere, *J. Geophys. Res.*, *103*(A2), 2261–2277, doi:10.1029/97JA03031.
- Tu, J., J. L. Horwitz, and T. E. Moore (2005), Simulating the cleft ion fountain at polar perigee altitudes, *J. Atmos. Sol. Terr. Phys.*, *67*(5), 465–477, doi:10.1016/j.jastp.2004.11.009.
- Tu, J. N., J. L. Horwitz, P. Song, X. Q. Huang, B. W. Reinisch, and P. G. Richards (2003), Simulating plasmaspheric field-aligned density profiles measured with IMAGE/RPI: Effects of plasmasphere refilling and ion heating, *J. Geophys. Res.*, *108*(A1), 1017, doi:10.1029/2002JA009468.
- Tu, J. N., J. L. Horwitz, P. A. Nsumei, P. Song, X. Q. Huang, and B. W. Reinisch (2004), Simulation of polar cap field-aligned electron density profiles measured with the image radio plasma imager, *J. Geophys. Res.*, *109*, A07206, doi:10.1029/2003JA010310.
- Webb, P., and E. Essex (2004), A dynamic global model of the plasmasphere, *J. Atmos. Sol. Terr. Phys.*, *66*(12), 1057–1073, doi:10.1016/j.jastp.2004.04.001.
- Wilson, G. R., J. L. Horwitz, and J. Lin (1992), A semikinetic model for early stage plasmasphere refilling: 1, Effects of Coulomb collisions, *J. Geophys. Res.*, *97*(A2), 1109–1119, doi:10.1029/91JA01459.
- Wu, X. Y., J. L. Horwitz, G. M. Estep, Y. J. Su, D. G. Brown, P. G. Richards, and G. R. Wilson (1999), Dynamic fluid-kinetic (DyFK) modeling of auroral plasma outflow driven by soft electron precipitation and transverse ion heating, *J. Geophys. Res.*, *104*(A8), 17,263–17,275, doi:10.1029/1999JA900114.
- Wu, X. Y., J. L. Horwitz, and J. N. Tu (2002), Dynamic fluid kinetic (DyFK) simulation of auroral ion transport: Synergistic effects of parallel potentials, transverse ion heating, and soft electron precipitation, *J. Geophys. Res.*, *107*(A10), 1283, doi:10.1029/2000JA000190.